Materials Chemistry and Physics 280 (2022) 125710

Contents lists available at ScienceDirect

Materials Chemistry and Physics

journal homepage: www.elsevier.com/locate/matchemphys

Interface matters: Design of an efficient α-Ag_2WO_4/Ag_3PO_4 photocatalyst

Aline B. Trench [a], Roman Alvarez [a], Vinícius Teodoro [a], Letícia G. da Trindade [b], Thales R. Machado [a], Mayara M. Teixeira [a], Daniele de Souza [c], Ivo M. Pinatti [d], Alexandre Z. Simões [d], Yara Galvão Gobato [c], Juan Andrés [e], Elson Longo [a,*]

[a] CDMF – Department of Chemistry, Federal University of São Carlos, 13565-905, São Carlos, SP, Brazil
[b] Department of Chemistry, Sao Paulo State University, 17033-360, Bauru, SP, Brazil
[c] Department of Physics – Federal University of São Carlos, 13565-905, São Carlos, SP, Brazil
[d] Faculty of Engineering of Guaratinguetá, São Paulo State University UNESP, 12516-410, Guaratinguetá, SP, Brazil
[e] Department of Analytical and Physical Chemistry, University Jaume I, 12071, Castellón, Spain

HIGHLIGHTS

- α-Ag_2WO_4/Ag_3PO_4 heterojunctions were synthesized by the co-precipitation method.
- Heterojunction with 24-wt% α-Ag_2WO_4 degrades RhB (94.3%) in 5 min in visible light irradiation.
- Surface plasmon resonance effect by Ag nanoparticles promotes improvement in charge carrier separation.

GRAPHICAL ABSTRACT

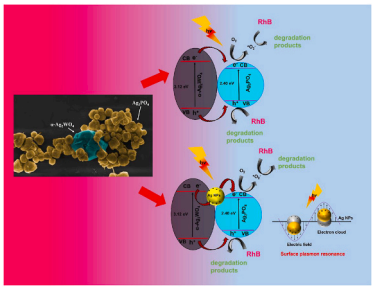

ARTICLE INFO

Keywords:
α-Ag_2WO_4/Ag_3PO_4
Photocatalytic activity
Surface plasmon resonance
Type I heterojunction

ABSTRACT

Heterojunction engineering of complex metal oxides is an active area of research that addresses fundamental questions in solid-state systems with broad technological applications. In this work, α-Ag_2WO_4/Ag_3PO_4 heterojunctions with different amounts of α-Ag_2WO_4 (12, 24, and 36 wt%) were synthesized by the coprecipitation method and characterized by X-ray diffraction, X-ray photoelectron spectroscopy, field emission scanning electron microscopy, transmission electron microscopy, UV–vis diffuse reflectance spectroscopy, and photoluminescence. The α-Ag_2WO_4/Ag_3PO_4 heterojunction containing 24% wt of α-Ag_2WO_4 showed the most enhanced photocatalytic activity for the degradation of Rhodamine B, being much higher than Ag_3PO_4 and α-Ag_2WO_4. Trapping experiments revealed that the holes and superoxide radical, in minor extent, were the main active species in the photocatalytic degradation. Such enhanced photocatalytic performance was explained by the surface plasmon resonance effect associated with the presence of metallic Ag at the interface and the formation of a type I heterojunction between α-Ag_2WO_4 and Ag_3PO_4 semiconductors.

* Corresponding author.
E-mail address: elson.liec@gmail.com (E. Longo).

https://doi.org/10.1016/j.matchemphys.2022.125710
Received 20 September 2021; Received in revised form 27 December 2021; Accepted 4 January 2022
Available online 10 February 2022

1. Introduction

Over the past few years, semiconductor photocatalysis has attracted much interest due the synthesis of innovative materials with excellent performance for organic pollutant degradation and waste water cleaning [1,2]. A highly efficient semiconductor needs to have a wide range of light absorption, a fast charge separation of photo-generated electron--hole (e^-—h^+) pairs and a strong redox ability [3–7]. However, it is difficult for a single-component photocatalyst to possess all these characteristics.

To overcome these drawbacks and improve the performance of a single semiconductor, in the last years two feasible methods emerged via a synergistic interaction/effect [8]. The firs refers to the formation of a heterojunction involving the combination of two or more semiconductors to form new materials [9–17]. This strategy constitutes a hotspot in recent research [1,18–24] to obtain new materials with superior electrical, optical, and catalytic properties associated with the transfer of interfacial charge and a synergistic effect between coupled semiconductors [25]. The second concerns the deposition of active metal nanoparticles (NPs) (for example, noble metals, such as Ag, Au or/and Cu nanoparticles), displaying localized surface plasmon resonance (SPR) effect on the semiconductor's surface [26,27]. In the first case, the photocatalytic activity of the heterojunction depends on the semiconductor type (p or n), chemical composition, band alignment, and location of valence/conduction band potentials.

The combination of metal and semiconductor significantly enhances the activity because of two main features: the formation of a Schottky barrier between the metal NPs, resulting in the increased separation efficiency of photogenerated (e^-—h^+) pairs [28]. The high electron trapping ability of NPs help to effectively promote the conductivity of NPs, which can then be directly injected into the conduction band of the semiconductors, facilitating the charge separation at the interface between NPs and the semiconductor, and consequently improving its photocatalytic ability [29–42].

The interface causes induced e^- and h^+ in or near this area to move in opposite directions, promoting charge transfer and suppressing the recombination of e^-—h^+ pairs, thus increasing their stability [43] and maximizing the redox power for heterojunction photocatalysts. This quantum phenomenon occurs in a confined region and is capable of enhancing the simultaneous (successive or parallel) transformation of compounds. As it occurs in other Ag-based semiconductors, both Ag_3PO_4 and α-Ag_2WO_4 are unstable and tend to segregate Ag metal nanoparticles (Ag NPs) on the surfaces of these complex oxides, hence forming Ag NPs/Ag_3PO_4 and Ag NPs/α-Ag_2WO_4 composites, respectively. These composites present SPR effect associated with the easy formation of Ag NPs on the surface of these semiconductors [30,32,37,41,44–48].

Despite the practical importance of such composites and the fact that they have been observed for different types of heterojunction [49], so far there is a lack of studies in the literature on a consistent pattern demonstrating the synergistic influence of plasmons of Ag NPs on their photocatalytic activity. Inspired by the unique properties of both Ag_3PO_4 and α-Ag_2WO_4, it was envisaged that the coupling of the heterojunction of both materials with presence of Ag NPs at the interface could provide additional active sites, significantly improving their photocatalytic property. Therefore, the aim of the present work was to obtain a α-Ag_2WO_4/Ag_3PO_4 heterojunction via a facile coprecipitation method in order to contribute to the discussions on the topic. To this end, a wide range of α-Ag_2WO_4 compositions (12, 24, and 36 wt%) was used. The as-synthetized heterojunctions were fully characterized by X-ray diffraction (XRD), X-ray photoelectron spectroscopy (XPS), transmission electron microscopy (TEM), field emission gun scanning electron microscopy (FE-SEM) and diffuse reflectance spectroscopy in the ultraviolet–visible region (UV–vis). This work can also provide important understanding on the role played by Ag NPs at the interface of these heterojunctions during the photocatalytic process of Rhodamine B (RhB) dye degradation. After systematically characterizing and evaluating the properties of the photocatalyst, it was possible to observe that this heterojunction exhibited higher photoactivity than pure counterparts. Based on the scavenger results, the photocatalytic mechanism was proposed and discussed in detail. Finally, the stability of the material was studied via recycling and reusability experiments.

2. Experimental section

2.1. Synthesis

Ag_3PO_4 sample was synthesized by the coprecipitation method in aqueous medium at 30 °C. 50 mL of deionized water and $(NH_4)_2HPO_4$ salt (0.001 mol) (98.6%, JT Baker) were added to a beaker. This solution was stirred at 30 °C for 10 min for complete salt dissolution. In another beaker, the same procedure was performed using 50 mL of deionized water and $AgNO_3$ salt (0.003 mol) (99.8%, Vetec). After salt dissolution, the solution containing $AgNO_3$ was added to the $(NH_4)_2HPO_4$ solution and kept under stirring for 10 min at 30 °C. Subsequently, the formed precipitate was washed with deionized water to remove residual ions, and then dried in a conventional oven at 60 °C for 12 h.

The α-Ag_2WO_4 crystals were also prepared by the coprecipitation method at room temperature. $Na_2WO_4{\cdot}2H_2O$ (0.007 M) (99.5%, Sigma-Aldrich) and $AgNO_3$ (0.0035 M) (99.8%, Sigma Aldrich) were stirred separately in a solution containing 50 mL of deionized water at room temperature until the complete dissolution of the salts. Afterwards, the $AgNO_3$ solution was added to the Na_2WO_4 solution and stirred for 10 min. The formed precipitate was washed with deionized water to remove residual ions, and then dried in a conventional oven at 60 °C for 12 h.

Stoichiometric contents of precursors reagents for α-Ag_2WO_4 and Ag_3PO_4 were used to obtain α-Ag_2WO_4/Ag_3PO_4 heterojunction with 12, 24 and 36 wt% of α-Ag_2WO_4 in relation to Ag_3PO_4, which were denominated as AWP 1, AWP 2 and AWP 3, respectively. For this purpose, α-Ag_2WO_4 was dispersed in a beaker containing 20 mL of deionized water at 30 °C under constant agitation. In another beaker, $(NH_4)_2HPO_4$ salt was dissolved in 20 mL of deionized water at 30 °C under constant stirring. This solution was added to the beaker containing the dispersed α-Ag_2WO_4 and kept under stirring at 30 °C for 10 min. Another solution was prepared using 20 mL of deionized water and $AgNO_3$, which was dissolved under stirring at 30 °C. This solution was dripped onto the suspension containing α-Ag_2WO_4 and $(NH_4)_2HPO_4$, and the whole mixture was stirred for 10 min. The precipitate formed was washed with deionized water to remove residual ions, and then dried in a conventional oven at 60 °C for 12 h.

2.2. Characterization

The obtained materials were characterized by XRD diffraction using a D/Max-2500PC diffractometer (Rigaku, Japan) with CuKα radiation (λ = 1.54056 Å) in the 2θ range of 10°–80° at a scanning speed of $1°min^{-1}$ and step size of 0.02°. Transmission electron microscopy (TEM) was performed using a FEI Tecnai G2F20 (Netherlands) microscope operating at 200 kV. Dark field (DF) image as well as local compositional analyses and mapping via energy-dispersive X-ray spectroscopy (EDS) were recorded in the scanning TEM (STEM) mode. The morphologies of the samples were characterized by field emission gun scanning electron microscopy (FE-SEM) in a FEI instrument (Inspection Model F50) operating at 10 kV.

Measurements of X-ray photoelectron spectroscopy (XPS) were performed on a Scientia Omicron ESCA + (Germany) spectrometer using monochromatic Al Kα (1486.7 eV). The maximum deconvolution was performed using a Gaussian (70%)–Lorentzian (30%) line with Shirley nonlinear sigmoid-type baseline. For calibration of the binding energy of the elements, peak C 1s at 248.8 eV was used as a reference. To obtain ultraviolet–visible (UV–vis) absorption spectra, a Varian Cary 5G

(United States) spectrophotometer was used in diffuse reflection mode.

Photoluminescence (PL) measurements were performed by using a 500 M SPEX spectrometer coupled to a GaAs-PMT detector. A Kimmon He–Cd laser (325 nm line) was used as excitation source. The PL measurements were performed in the range of 380–750 nm with laser power of about 16 mW and at 300 K.

2.3. Photocatalytic measurements

The photocatalytic activity of Ag_3PO_4, α-Ag_2WO_4 and heterojunction samples AWP 1, AWP 2 and AWP 3 were tested for Rhodamine B (RhB) discoloration (95%, Aldrich) under visible light irradiation. For the photocatalytic experiments, 50 mg of each sample and 50 mL of RhB (10 mg L^{-1}) were placed in a beaker, and later in an ultrasonic bath (Branson, model 1510; frequency 42 kHz) for 15 min, followed by stirring for another 30 min, always keeping samples in the dark. An aliquot was collected at time 0, and the RhB solution containing the catalyst was exposed to the irradiation of 6 lamps (Philips TL-D, 15 W). The entire system was maintained at a constant temperature of 20 °C. Aliquots were removed at certain times (0, 2, 5, and 10 min). All aliquots were centrifuged, and their degradation was monitored by measuring the peak of maximum RhB absorption (λ_{max} = 554 nm) using a UV–visible spectrophotometer (V-660, JASCO). A control experiment was carried out under the same conditions, but without the presence of catalysts.

To elucidate the mechanism of α-Ag_2WO_4/Ag_3PO_4 photocatalytic activity enhancement, the main active species that participated in the photocatalytic reaction were investigated. The free radicals and holes trapping experiments were carried out. The scavenger experiments were performed by the addition of *tert*-butyl alcohol (TBA, 0,012 mol/L) (Alfa Aesar), ammonium oxalate (AO, 0.012 mol/L) (Alfa Aesar) and benzoquinone (BQ, 0.012 mol/L) (Alfa Aesar) as scavengers of hydroxyl radical (•OH), hole (h^+) and superoxide radical ($\bullet O_2^-$), respectively.

3. Results and discussion

3.1. Powders characterization

The Ag_3PO_4 and α-Ag_2WO_4 were synthesized by the coprecipitation method, as previously reported [50,51]. The heterojunctions containing 12, 24 and 36 wt% of α-Ag_2WO_4 in relation to Ag_3PO_4 were synthesized as shown in Fig. 1, and denoted as AWP 1, AWP 2 and AWP 3, respectively.

Fig. S1, in Supplementary Information, shows the XRD patterns of the Ag_3PO_4, AWP 1, AWP 2, AWP 3 and α-Ag_2WO_4 samples. The XRD pattern of the Ag_3PO_4 sample are in good agreement with the Inorganic Crystal Structure Database (ICSD) No. 14000, with a cubic structure and $P\bar{4}3n$ space group [52]. On the other hand, the α-Ag_2WO_4 sample has an orthorhombic structure with a *Pn2n* space group, according to ICSD No. 4165 [53].

It was observed that as the amount of α-Ag_2WO_4 increased, the XRD peaks referring to this phase intensified, which is well expected due to the higher content of this material. No characteristic peaks related to any impurities or secondary phase were noted, suggesting that the samples presented only α-Ag_2WO_4 and Ag_3PO_4 phases.

TEM analysis was performed for the sample with an intermediate amount of α-Ag_2WO_4 (AWP 2). Fig. 2(a) shows a low-magnified DF-STEM image, where two main arrangement of particles in this sample comprising faceted nanospheres and elongated irregular microparticles covered by these nanospheres can be seen. Fig. 2(b) shows a magnified view corresponding to the dotted square marked in Fig. 2(a). An elemental characterization by EDS was conducted in the microparticle and nanospheres, as shown in Fig. 2(b). The resulting EDS spectrum for the microparticle indicates the predominance of the elements Ag, P, W and O, whereas the irregular nanospheres are mainly composed of Ag, P and O. Fig. 2(c–f) show the EDS mapping of the elements Ag, P, W and O corresponding to the region in (b), again confirming the presence of the elements referring to the heterojunction and the homogeneity of the sample.

To complement this result, selected area electron diffraction (SAED) analyses (insets in Fig. 3) were conducted in the same region of Fig. 2 (b), and as indicated by the dotted arrows they reveal patterns typically observed in polycrystalline materials. The nanospheres exhibit concentric rings that can be indexed to the (220), (310), and (520) families of planes of the cubic Ag_3PO_4, while the patterns on the elongated microparticle reveal the presence of both (402) and (633) families of planes of the α-Ag_2WO_4 structure, and (233) family of planes associated with the Ag_3PO_4 structure. These results confirm the successful formation of Ag_3PO_4 nanospheres and their crystallization on the surface of α-Ag_2WO_4 microcrystals, forming the heterojunction.

Fig. 4 shows the micrographs of the pure materials and the heterojunction formed in different proportions. The Ag_3PO_4 structure, represented by the orange color, exhibits a morphology with irregular nanospheres (Fig. 4(a)), while the α-Ag_2WO_4 structure, represented by the blue color, displays a morphology with hexagonal microrods (Fig. 4 (b)). In the heterojunction (Fig. 4(c–e)), it can be seen that the interaction of the materials during the synthesis process causes changes in the morphology of both materials. As presented in the TEM analysis, the elongated irregular blue microparticle is composed of the α-Ag_2WO_4 structure, whereas the smaller nanosphere orange particles are formed by the Ag_3PO_4 structure. The change in the morphology of the heterojunction is due to the dissolution and recrystallization of the rods in aqueous medium, which consequently formed larger faceted microparticles. Sample AWP1 showed an agglomerate of particles that coalesced to form a large microparticle represented by the blue color, which can be attributed to the α-Ag_2WO_4 structure (Fig. 4(c)). Samples AWP2 and AWP3, on the other hand, were characterized by the presence of large microparticles with well-defined surfaces (Fig. 4(d–e)). EDS results revealed that the α-Ag_2WO_4 microparticles were covered by the elements Ag, P and O, with the smaller nanoparticles corresponding to the Ag_3PO_4 structure. Moreover, the Ag_3PO_4 nanoparticles presented more defined surfaces in the heterojunction.

To investigate the chemical composition and surface structure of the as-prepared samples, XPS measurements were carried out. The analysis

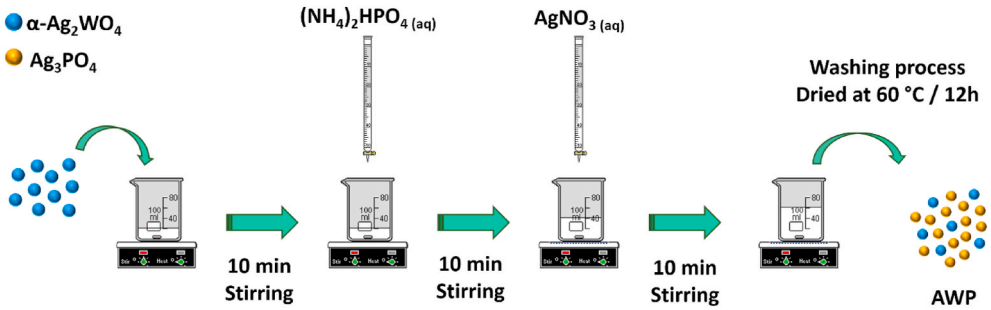

Fig. 1. Schematic representation of the synthesis procedure.

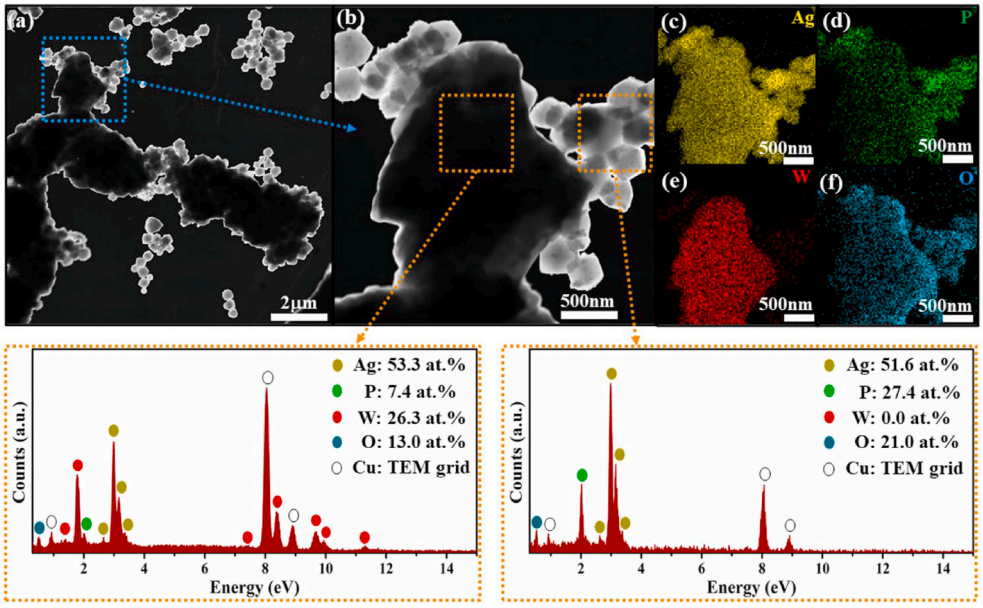

Fig. 2. TEM characterization of sample AWP 2: (a) DF-STEM image, (b) high-magnification DF-STEM image and EDS spectra obtained at Ag_3PO_4 crystallized on α-Ag_2WO_4 surface, and (c–f) EDS mapping of the elements Ag, P, W, and O corresponding to the region in (b).

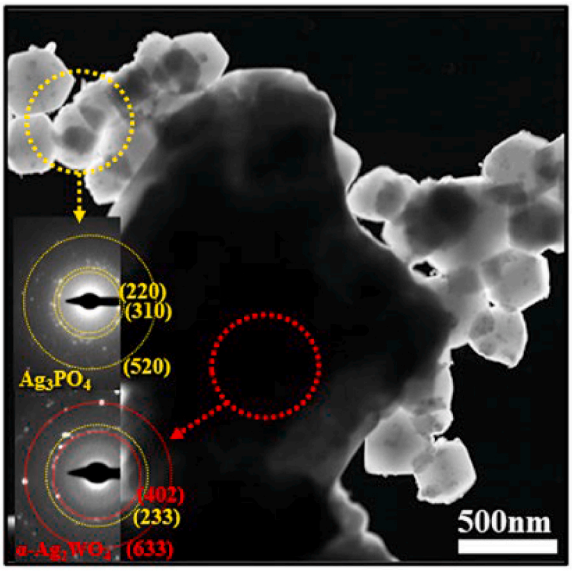

Fig. 3. DF-STEM image and its corresponding SAED patterns of sample AWP 2.

of the high-resolution spectra of the constituent elements of α-Ag_2WO_4 and Ag_3PO_4 samples is presented in Fig. S2, in Supplementary Information. The deconvolution analysis of the P 2*p* spectrum of Ag_3PO_4 as well the W 4*f* spectrum of α-Ag_2WO_4 indicates the presence of P^{5+} and W^{6+} oxidation states, as shown in Fig. S2(b) and Fig. S2(e), respectively [54,55]. The deconvolution analysis of the Ag 3*d* spectra for both Ag_3PO_4 and α-Ag_2WO_4 samples reveals the presence of Ag^+ and Ag^0 oxidation states according to their respective spin-orbit coupling peaks, as demonstrated in Fig. S2(a) and Fig. S2(d), respectively [56–58]. Fig. S2(c) and Fig. S2(f) show the O 1*s* spectra for the Ag_3PO_4 and α-Ag_2WO_4 samples, respectively, and their components for lattice oxygen (≈530 eV), oxygen vacancies (≈531.5 eV) and hydroxyl-bounded groups on particle surface (≈533 eV) [59,60].

The heterojunction with intermediate amount of α-Ag_2WO_4 (AWP 2) was investigated by XPS. The Ag 3*d* spectrum of sample AWP 2 is shown in Fig. 5(a), where it is possible to see well-defined components of the spin-orbit coupling related to both Ag^+ and Ag^0 oxidation states. The contribution of the Ag^0 oxidation state arises from the presence of metallic Ag nanoparticles on the surface of Ag_3PO_4 and α-Ag_2WO_4 particles that results in Ag metal/semiconductor interface. The deconvolution analysis of the P 2*p* spectrum for AWP 2 indicates the presence of P^{5+} oxidation state (Fig. 5(b)). The O 1*s* spectrum for AWP 2 together with its main components and the survey spectra for Ag_3PO_4, α-Ag_2WO_4 and AWP 2 are shown in Fig. 5(c) and (e), respectively. Variations in the broadening of the peaks of W 4*f* spectrum for AWP 2 in relation to pure α-Ag_2WO_4 can be observed in Fig. 5(d) by the broadening of the peaks. The deconvolution results indicated the presence of two oxidation states for W in this sample: W^{6+} in major proportion and W^{5+} in minor proportion. The presented components were attributed to the spin-orbit coupling of W^{6+} $4f_{7/2}$ (35.9 eV) and W^{6+} $4f_{5/2}$ (38.0 eV), W^{5+} $4f_{7/2}$ (35.0 eV) and W^{5+} $4f_{5/2}$ (37.2 eV) [61], and a shoulder related to the W^{6+} loss feature (41.2 eV).

Several works have reported the effects of heterojunction formation in the surface structure of the materials, such as interfacial strain [62–65]. The presence of W^{5+} in sample AWP 2 can be attributed to interfacial strain due to lattice mismatch between α-Ag_2WO_4 and Ag_3PO_4 since this latter was grown upon α-Ag_2WO_4 particles. Furthermore, the W^{6+} reduction can be assigned to the charge transfer effect between α-Ag_2WO_4 and Ag_3PO_4 caused by the effective formation of the heterojunction that leads to the energy level alignment [66].

It is well known that the photocatalytic activity of the photocatalysts is closely related to their light absorption ability. In this way, UV–vis diffuse reflectance spectroscopy was employed to determine the optical absorption properties of the pure Ag_3PO_4, α-Ag_2WO_4, and α-Ag_2WO_4/Ag_3PO_4 heterojunction. The results are represented in Fig. 6. The Ag_3PO_4 and α-Ag_2WO_4 samples show an absorption edge in the visible region at 510 nm and 405 nm, respectively. It was observed in the heterojunction samples (AWP 1, AWP 2 and AWP 3) that the spectra have two absorption edge wavelengths near these absorption edges, proving the presence of both materials, and therefore the successful formation of the heterojunction. It was also noted a slight redshift in the absorption edge at 405 nm referring to α-Ag_2WO_4, which favors the use of visible light in the photocatalytic process.

The band gap energy (E_g) of the α-Ag_2WO_4 and Ag_3PO_4 samples (Fig. S3) were calculated using the Tauc method, following Equation (1) [67],:

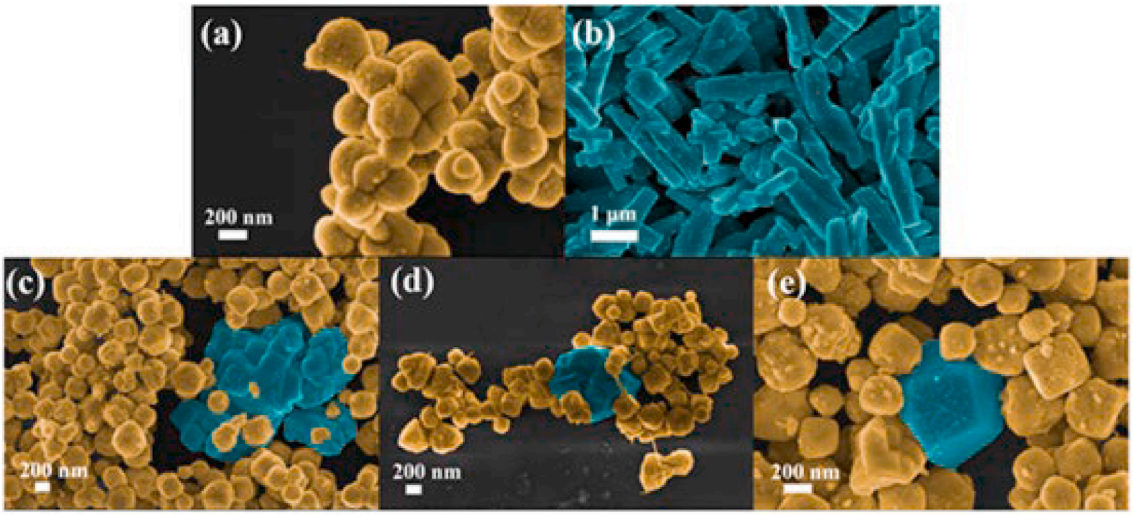

Fig. 4. FE-SEM images of (a) Ag_3PO_4 (orange color), (b) α-Ag_2WO_4 (blue color), (c) AWP 1, (d) AWP 2 and (e) AWP 3. (For interpretation of the references to color in this figure legend, the reader is referred to the Web version of this article.)

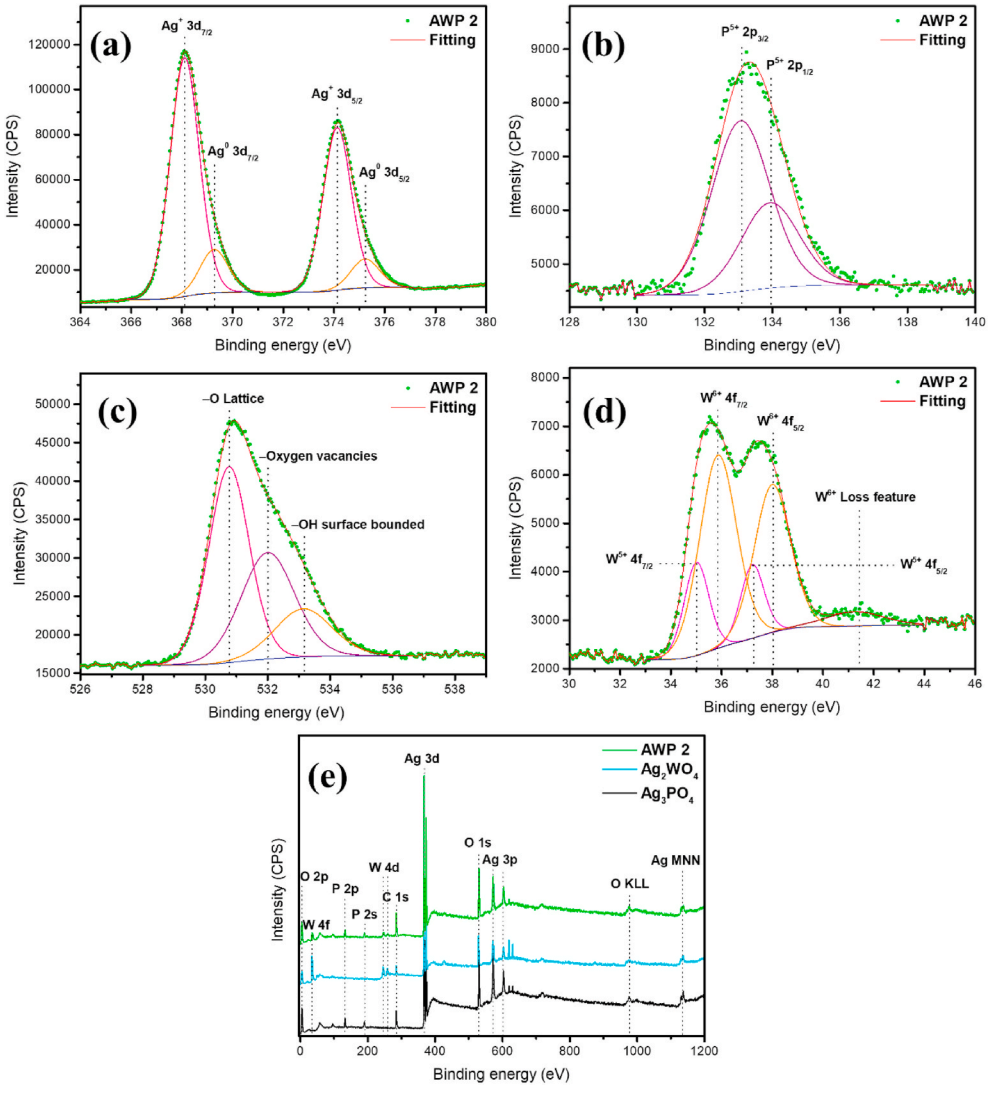

Fig. 5. High-resolution XPS spectra of (a) Ag 3*d*, (b) P 2*p*, (c) O 1*s* and (d) W 4*f*, and (e) survey of AWP 2, α-Ag_2WO_4, and Ag_3PO_4.

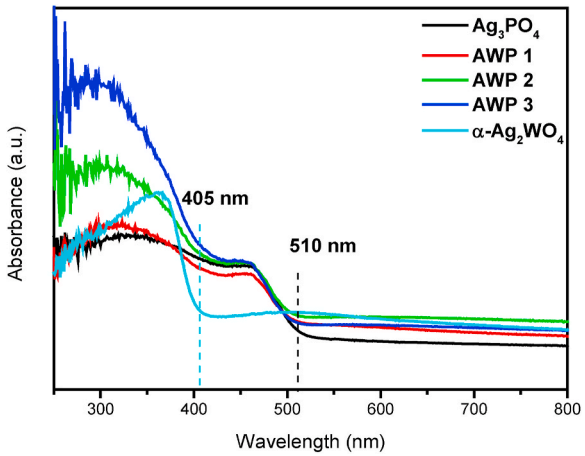

Fig. 6. UV–vis diffuse reflectance spectra of Ag_3PO_4, AWP 1, AWP 2, AWP 3 and α-Ag_2WO_4.

$$(\alpha h\nu)^{2/n} \sim \left(h\nu - E_g\right) \quad (1)$$

where $n = 1$ for a semiconductor with direct band gap, $n = 4$ for a semiconductor with indirect band gap, α = absorbance, and $h\nu$ is photon energy. Ag_3PO_4 has an indirect band gap ($n = 4$) [68] with an experimental E_g value of 2.40 eV, as shown in Fig. S3(a). The calculated E_g value is in agreement with those reported in the literature [69]. Fig. S3 (b) shows the experimental band gap of α-Ag_2WO_4, which has direct band gap ($n = 1$) [70] with a value of 3.12 eV. This experimental E_g value is also in well agreement with those reported in the literature [71].

The photoluminescence (PL) spectrum is usually employed to investigate the separation and transfer efficiency of the photogenerated (e^-—h^+) pairs during the photocatalytic process [72]. It is well known that the stronger PL intensity indicates the faster recombination speed of photogenerated charge carriers, implying that fewer photoinduced e^- and h^+ took part in the photocatalytic oxidation and reduction reactions, resulting in lower photocatalytic activity [73]. Fig. 7 exhibits the PL spectra of the as-prepared samples under the excitation wavelength of 325 nm. An analysis of the results renders that the PL spectrum of Ag_3PO_4 presents a broadband profile with the maximum emission intensity in the blue region of the visible electromagnetic spectrum at around 454 nm (2.731eV), which is in agreement with the previous results reported in the literature [46,74]. This emission occurs mainly by the charge transfer (e^-—h^+) process between the different clusters that compose the material, such as [PO_4] tetrahedron clusters [46,68,75]. On the other hand, the α-Ag_2WO_4 sample showed a PL intensity peak also in the blue region centered at 456 nm (2.719eV), and another emission in the red region with a maximum emission intensity between 570 and 650 nm (about 1.984 eV). The blue emission peak is usually related to distorted [WO_6] octahedron, while the emission in the red region can be assigned to [AgO_y] clusters with y = 2, 4, 6 and 7, which arise from oxygen vacancies in the semiconductor [76,77]. The heterojunction samples also showed emissions in the blue region at approximately 451 nm, which are close to the blue emission from the isolated materials. Particularly, samples AWP 1 and AWP 2 exhibited a broadband profile similar to Ag_3PO_4, while AWP 3 had a profile similar to α-Ag_2WO_4. This result could be associated with the fact that AWP 3 has a higher amount of α-Ag_2WO_4, resulting in a band profile similar to α-Ag_2WO_4. It can then be concluded that the PL results are consistent with the charge transfer processes of carriers between Ag_3PO_4 and α-Ag_2WO_4 semiconductors in the heterojunction.

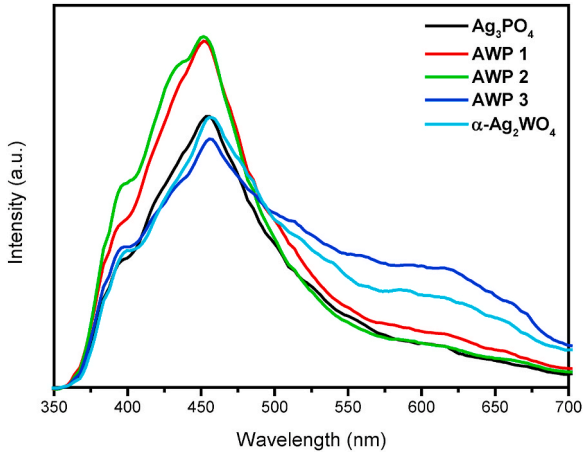

Fig. 7. PL spectra of Ag_3PO_4, AWP 1, AWP 2, AWP 3 and α-Ag_2WO_4 at 300 K.

According to the interfacial strain resulting from synergetic effects, it was possible to observe that the α-Ag_2WO_4 presented surface defects, such as a mix of W^{5+} and W^{6+} oxidation states (suggested by XPS experimental results), leading to a higher proportion of distorted [WO_6] clusters in the heterojunction. This caused the charge recombination related to these defects to increase, resulting in a higher emission in the blue region (around 454 nm) for samples AWP 1 and AWP 2, which showed higher PL intensities than the other samples. Additionally, the e^-—h^+ recombination rate in Ag_3PO_4 could be decreased, boosting its photocatalytic performance for oxidative reactions.

3.2. Photocatalytic activity

The photocatalytic performance of α-Ag_2WO_4, Ag_3PO_4 and heterojunction samples AWP 1, AWP 2 and AWP 3 were investigated for the photodegradation of RhB dye under visible light irradiation. The degradation process was monitored by UV–vis absorption spectra at 554 nm, and the degradation curves are displayed in Fig. 8. Tests on the RhB adsorption process of all samples were performed and the results are presented Fig. S4. For this, after a period of 15 min in the ultrasound bath, the samples were under constant agitation (in the dark) for 30 min, with aliquots being removed every 10 min in order to evaluate the absorption profiles of the samples. An analysis of the results shows that the absorbance profiles are no dependent of the adsorption process. The Ag_3PO_4 sample showed a higher photocatalytic activity than α-Ag_2WO_4, degrading approximately 70% of the dye in 10 min of reaction, while for the latter no dye degradation was observed in the same reaction time. This low photocatalytic activity of α-Ag_2WO_4 can be attributed to the use of visible light since the material has a band gap energy that corresponds to excitation in the UV region (Fig. S3(a)). As a consequence, e^- cannot be excited from the valence band (VB) to the conduction band (CB) [78]. Conversely, Ag_3PO_4 has a band gap energy that corresponds to excitation in the visible region, generating e^-—h^+ pairs under visible light irradiation, consequently degrading the dye. This makes Ag_3PO_4 a promising photocatalyst compared to α-Ag_2WO_4, as it has the possibility of using sunlight irradiation for the degradation of organic compounds. The degradation curves for the heterojunction are also shown in Fig. 8. It can be noted that all samples presented a photocatalytic activity superior to that of the isolated materials, demonstrating that the synergistic effect was effective for the formation of a heterojunction interface, responsible for the charge carrier transfer.

To investigate the kinetics of the RhB photodegradation reaction, the Langmuir-Hinshelwood model [15] was used, considering a pseudo-first order reaction, according to equation -ln (C_N/C_0) = kt, where C_N and C_0 represent the RhB concentration at different time intervals and in the initial stage, respectively, and k and t represent the rate constant and irradiation time correspondingly, respectively. Fig. 9(a) displays the variations in RhB concentration as C_N/C_0 *versus* irradiation time for the different samples. The photolysis experiment performed is illustrated in Fig. 8(a), where no degradation can be seen. Fig. 9(b) shows the values found for the rate constants (k) using the Langmuir-Hinshelwood model

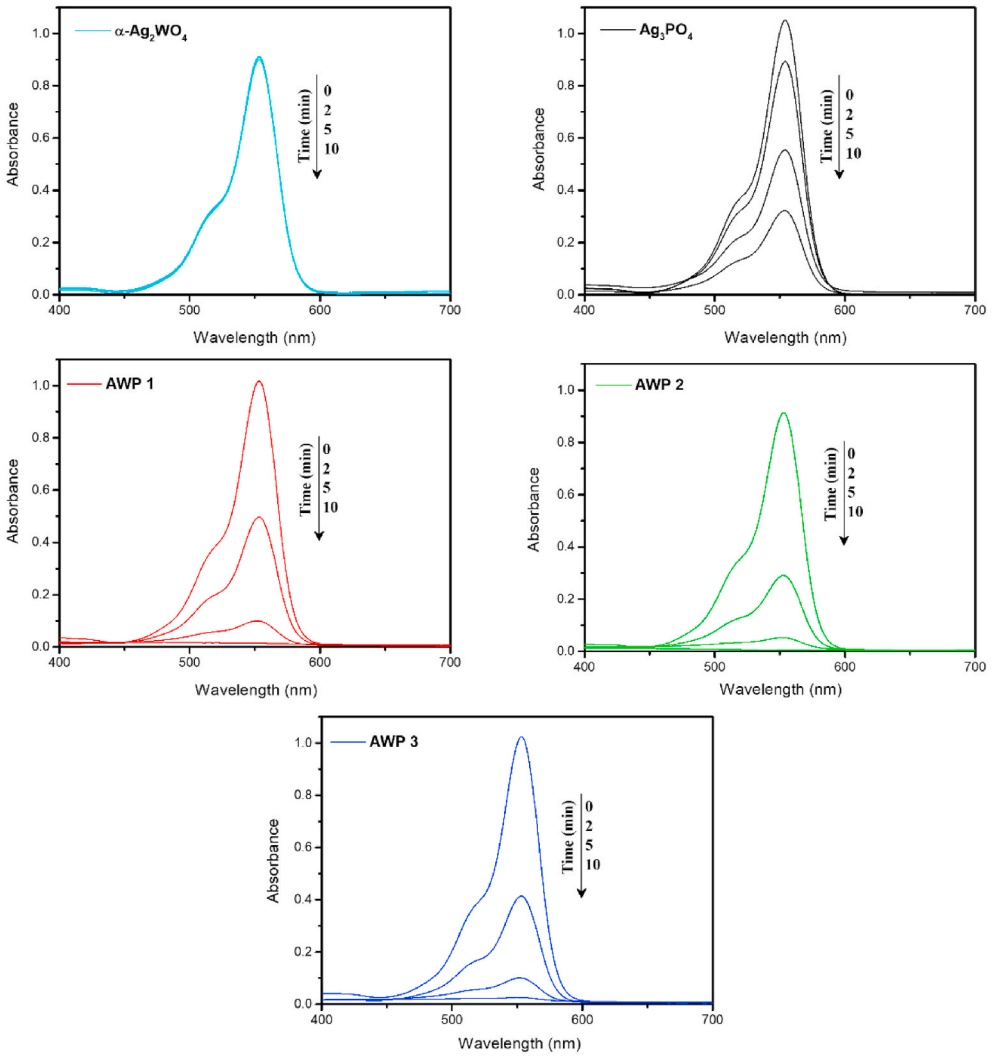

Fig. 8. UV–vis absorbance plots for RhB photocatalytic degradation in the presence of 50 mg of each catalyst and 50 mL of RhB (10 mg L^{-1}).

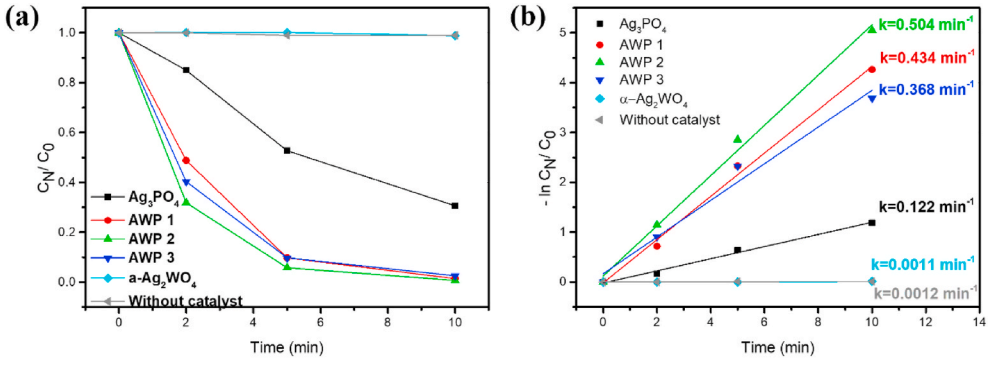

Fig. 9. Photocatalytic degradation (a) and kinetic fit curves for all samples under visible-light irradiation (b).

abovementioned. It was observed that the heterojunction presented k values higher than those of isolated materials, especially sample AWP 2, which reached a value 4.13 times higher than that of Ag_3PO_4 and 458 times higher than of α-Ag_2WO_4, being the sample with the highest photocatalytic activity.

Note that the increased value of k in AWP 2 with respect to AWP 1 may have been due to the greater amount of α-Ag_2WO_4 inserted into the sample, which increased the synergistic effect between α-Ag_2WO_4 and Ag_3PO_4, enhancing the transfer of charge carriers and improving the photocatalytic activity of AWP 2. The value of k for AWP 3 possibly decreased in relation to AWP 2 as a result of the highest amount of α-Ag_2WO_4 contained in this sample in relation to the other heterojunction, thus requiring a higher proportion of UV light for the separation of the charge carriers, lowering its photocatalytic activity – which was still higher than that of isolated materials since the synergistic effect between the Ag_3PO_4 and α-Ag_2WO_4 samples prevailed. In addition, the excess of α-Ag_2WO_4 in sample AWP 3 caused a competition between the active sites and Ag_3PO_4 for the adsorption of species.

Table 1 shows the photocatalytic efficiency of the α-Ag_2WO_4/Ag_3PO_4 heterojunction synthesized in this work in comparison with other studies that used modified Ag_3PO_4 or the composite coupled to another material for RhB photodegradation. The data presented in Table 1 indicate that α-Ag_2WO_4/Ag_3PO_4 heterojunction in this work has a remarkably higher efficiency for RhB degradation, being the material with the highest rate constant among those reported there. Although Li et al. [79] synthesized an α-Ag_2WO_4/Ag_3PO_4 heterostructure for the photodegradation of bisphenol A, however without mentioning the presence of metallic silver in its heterostructure, this is the first time that the α-Ag_2WO_4/Ag_3PO_4 heterojunction in the presence of Ag NPs is studied for RhB photodegradation under visible light irradiation.

To evaluate the stability and reuse of the photocatalyst, recycling experiments were carried out under identical conditions using the sample with the highest photocatalytic activity (AWP 2). Fig. 10 displays the five cycles performed for the RhB photodegradation. It can be noted that the first three cycles are relatively stable, with a catalyst deactivation of approximately 27% and 47% only in the fourth and fifth cycles, respectively. This decrease in the photocatalytic activity of AWP 2 may be related to the photocorrosion process that the sample is susceptible, which is a well-known phenomenon in Ag-based materials. To confirm the photocorrosion effect, the analysis of the XRD patterns of the AWP 2 sample was performed after the fifth cycle of the photocatalytic experiment and the results are presented in Fig. S5. Note that the formation of a peak located at $2\theta = 38.1°$, which corresponds to the (111) diffraction plane of Ag^0 (JCPDS Card nº 89–3722). It is believed that the loss in photocatalytic activity after the third cycle is related to the increase in the production of Ag^0, since the excess of Ag^0 formed in the material decreases the light absorption, and then its performance.

In this study, trapping experiments were performed in sample AWP 2 to investigate the main reactive species (Fig. 11). The scavenger experiments for $\bullet O_2^-$, •OH and h^+ were investigated by using the capture agents 1,4-benzoquinone (BQ), *t*-butyl alcohol (TBA) and ammonium oxalate (AO), respectively [87]. Meanwhile, the RhB degradation process was inhibited by the addition of AO; however, when BQ was added, this process was moderately suppressed, i.e., the photocatalytic rate was reduced to 48%. Furthermore, no inhibition was detected when using TBA, indicating that •OH does not contribute to the degradation of RhB. These results demonstrate that h^+ and $\bullet O_2^-$, in minor extent, are the main active species participating in the dye degradation ($h^+ > \bullet O_2^- \gg \bullet OH$). At this point, it is important to mention that the possible mechanism for the degradation process is very dependent not only on the antioxidant capacity of scavengers, but also on the nature of the radical chain reaction. The chain reactions involving $\bullet O_2^-$ radical participate in the degradation process, as occurred in the present case. The participation and generation of •OH along the degradation process does not rule, and the scavenging effect of BQ on $\bullet O_2^-$ radical tends to inhibit the formation of •OH radicals. In this case, the catalytic reaction rate will be greatly reduced by adding either BQ or TBA.

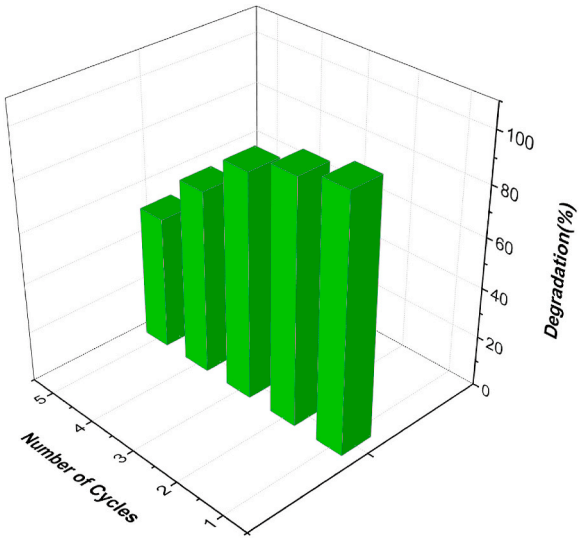

Fig. 10. The RhB photodegradation cycles using 50 mg of AWP 2 sample and 50 mL of RhB (10 mg L^{-1}) under visible light irradiation.

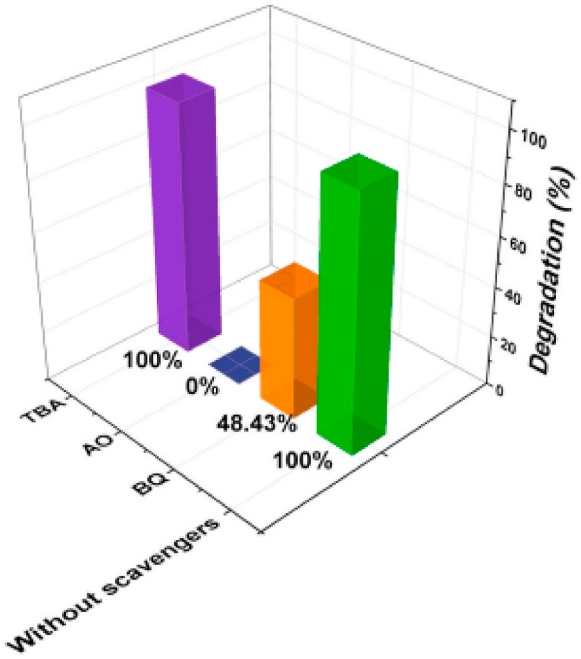

Fig. 11. Effect of scavengers on the degradation efficiency.

3.3. Possible photocatalytic mechanism

It is known that the mechanism for photocatalytic degradation is closely related to the position of the conduction (CB) and valence (VB) bands of a semiconductor. Thus, to fully understand the photocatalytic reaction mechanism occurring during the photodegradation of the as-

Table 1
Comparison of photodegradation of RhB using visible light by materials containing Ag_3PO_4 with the reported literature.

Catalyst	Mass of catalyst (mg)	RhB concentration (mg/L)	Rate constant (min^{-1})	Time degradation (min)	Reference
Ag_3PO_4/N–TiO_2	20	10	0.019	120	[80]
g-C_3N_4@Ag@ Ag_3PO_4	6	20	0.030	60	[81]
Ag_2MoO_4/Ag_3PO_4	50	10	0.359	12	[82]
Ag_3PO_4/NiO	30	5	0.224	30	[83]
$Ag_3PO_4/BiNbO_4$	15	20	0.146	30	[84]
Ag_3PO_4@$MgFe_2O_4$	20	10	0.1370	30	[85]
Ag_3PO_4:Mo	50	10	0.347	15	[50]
Ag_3PO_4:W	50	10	0.449	10	[86]
α-Ag_2WO_4/Ag_3PO_4	50	10	0.504	10	Our work

prepared α-Ag_2WO_4/Ag_3PO_4 heterojunction, the energy band edge positions of the VB and the CB of both α-Ag_2WO_4 and Ag_3PO_4 were calculated. The energy band diagram for the heterojunction was constructed using Equations (2) and (3), which are based on the Mulliken's electronegativity, i.e., the geometric mean of the electronegativity of the constituent atoms in the material composition (Hill notation) [88,89]:

$$E_{VB} = \chi - E_g + 0.5E_g \quad (2)$$

$$E_{CB} = E_{VB} - E_g \quad (3)$$

where E_{VB} is the valence band potential, E_{CB} is the conduction band potential, E_e is the free electron energy on the hydrogen scale (~4.5 eV), E_g is the semiconductor band gap energy (Fig. S3), and χ is the absolute electronegativity (Mulliken's electronegativity) of the semiconductor. For Ag_3PO_4, the value of χ is 5.96 eV [83], and for α-Ag_2WO_4 it is 6.00 eV [90]. Therefore, by employing Equations (2) and (3) the E_{VB} and E_{CB} values of 2.66 eV and 0.26 eV for Ag_3PO_4 and 3.06 eV and −0.06 eV for α-Ag_2WO_4, respectively, were obtained and are in agreement with those reported in the literature [91,92].

Fig. 12 illustrates two degradation mechanisms proposed for the α-Ag_2WO_4/Ag_3PO_4 heterojunction based on the obtained results. As shown in Fig. 12 (a), under visible light irradiation both Ag_3PO_4 and α-Ag_2WO_4 are excited, generating e^-—h^+ pairs. Due to the energy position of the CB and the VB of each material, a type I heterojunction is formed, the photoexcited e^- in the CB of α-Ag_2WO_4 migrates to the CB of Ag_3PO_4, and the photogenerated h^+ in the VB of α-Ag_2WO_4 also migrates to the VB of Ag_3PO_4, thus generating an accumulation of charge carriers in Ag_3PO_4. In the VB of Ag_3PO_4, the h^+ that comes from α-Ag_2WO_4 and the photogenerated h^+ in the Ag_3PO_4 can directly degrade RhB [86,93], as shown in Equation (4):

$$h^+ + \text{RhB} \rightarrow \text{degradation products} + CO_2 + H_2O \quad (4)$$

The as-mentioned reaction is in accordance with the observed scavenger results displayed in Fig. 11, which indicate that h^+ is the main species acting in the RhB photodegradation.

As the CB of Ag_3PO_4 (0.26 eV) is more positive than the potential of $O_2/{\bullet}O_2^-$ ($E^0(O_2/{\bullet}O_2^-) = -0.046$ eV vs. NHE) [94], from a theoretical point of view it can be concluded that the photoexcited e^- on Ag_3PO_4 cannot react with dissolved O_2 in the reaction solution to yield $\bullet O_2^-$. However, this reaction between the accumulated e^- on the Ag_3PO_4 surface with the adsorbed O_2 to produce $\bullet O_2^-$ have been reported in several recent studies [83,95,96]. As seen in Fig. 11, the $\bullet O_2^-$ species act, to a lesser degree, in the photodegradation of RhB, according to Equation (5):

$$\bullet O_2 + \text{RhB} \rightarrow \text{degradation products} + CO_2 + H_2O \quad (5)$$

As seen in the scavenger experiments (Fig. 11), the •OH species do not participate in the degradation mechanism, and a possible explanation is that •OH would be rapidly self-consumed, forming H_2O and O_2

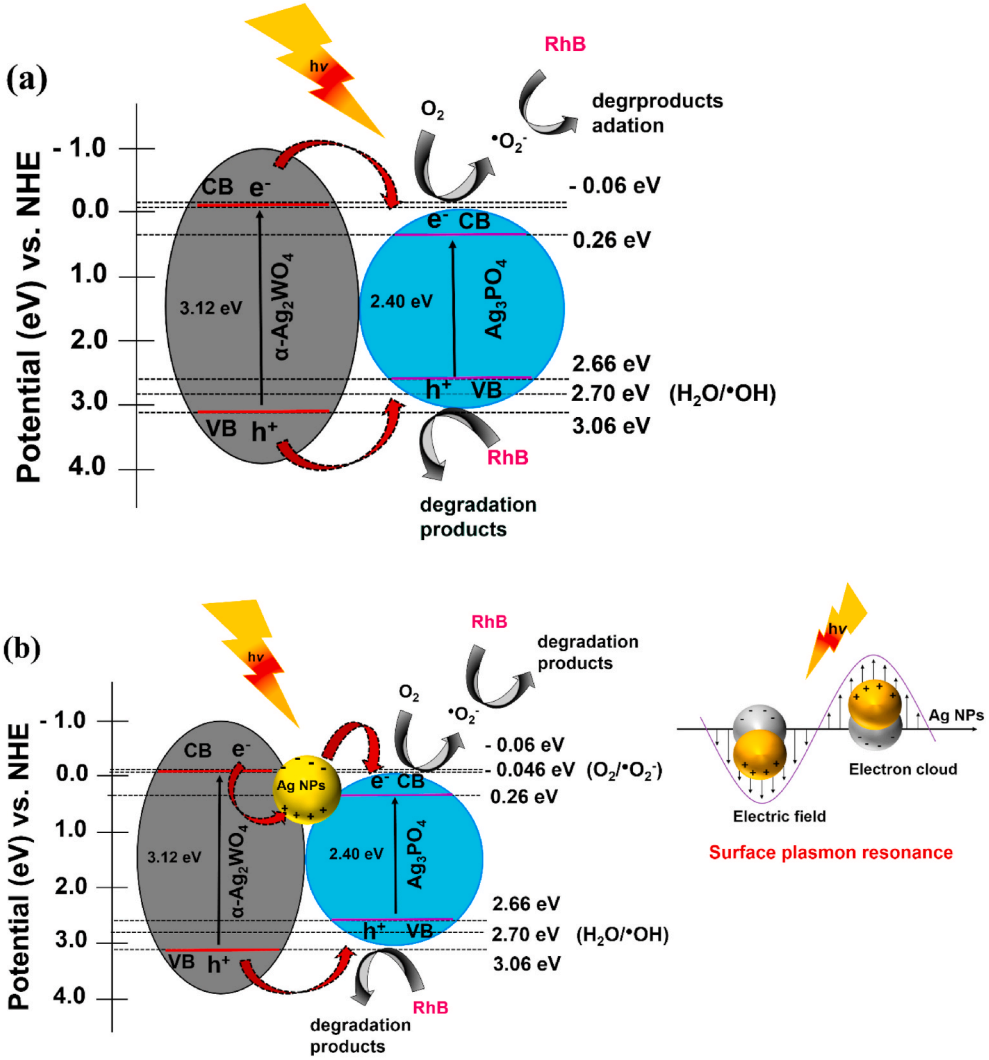

Fig. 12. Possible photocatalytic mechanism diagram.

[50], according to Equation (6):

$$4 \bullet OH \rightarrow 2H_2O + O_2 \quad (6)$$

As seen in XPS spectra results (Fig. 5), the Ag NPs formed may be present at the interface of the two semiconductors and could contribute to the separation process of e^-—h^+ pairs due to the surface plasmon resonance (SPR) effect, which creates a cross-linking bridge for both semiconductors [16]. The surface plasmon excitations are generated under visible light irradiation and partially converted into energetic electrons on the surface of Ag NPs. Fig. 12 (b) shows a proposed RhB degradation mechanism in the presence of Ag NPs, where it can be seen that the heterojunction remains type I and the same oxidizing species act. However, e^- photoexcited in α-Ag_2WO_4 can be transferred more quickly to Ag NPs. Thus, the e^- that are photoexcited to the CB of α-Ag_2WO_4 are able to migrate to the CB of Ag_3PO_4 more efficiently, as they use Ag NPs as a bridge. Therefore, the formation of metallic Ag NPs leads to an SPR effect, which is advantageous for the effective separation of charge carriers, resulting in improved photoactivity.

4. Conclusion

In conclusion, α-Ag_2WO_4/Ag_3PO_4 heterojunctions with different weight ratios of α-Ag_2WO_4 were fabricated by a facile chemical precipitation method. Under visible light irradiation, the as-prepared α-Ag_2WO_4/Ag_3PO_4 heterojunction displayed enhanced photocatalytic activity for the photocatalytic degradation of RhB. In particular, the sample with weight content of 24% of α-Ag_2WO_4 (named AWP 2) showed the highest photocatalytic performance for RhB photodegradation, degrading 94.3% in only 5 min of exposure to visible light, which is a very promising result when compared to pure Ag_3PO_4 and α-Ag_2WO_4 materials, which degraded 45 and 10%, respectively, under the same conditions. Our results demonstrate that this heterojunction can significantly enhance the absorption of visible light and successfully separate photogenerated electrons and holes after excitation. Such enhanced photocatalytic performance was explained by the surface plasmon resonance effect associated with the presence of metallic Ag at the metallic interface, as well as the formation of type I heterojunction, which served as a load transfer bridge, avoiding e^--h^+ recombination, and consequently improving the photocatalytic activity of the heterojunction since charge carriers are available to react with the adsorbed species for a longer time.

CRediT authorship contribution statement

Aline B. Trench: Conceptualization, Methodology, Validation, Formal analysis, Writing – original draft. **Roman Alvarez:** Conceptualization, Methodology, Validation, Formal analysis, Writing – original draft. **Vinícius Teodoro:** Investigation, Writing – original draft. **Letícia G. da Trindade:** Investigation, Writing – original draft. **Thales R. Machado:** Investigation, Writing – original draft. **Mayara M. Teixeira:** Investigation, Writing – original draft. **Daniele de Souza:** Investigation, Writing – original draft. **Ivo M. Pinatti:** Investigation, Writing – original draft. **Alexandre Z. Simões:** Conceptualization, Writing – review & editing, Supervision, Resources, Funding acquisition. **Yara Galvão Gobato:** Conceptualization, Writing – review & editing, Supervision, Resources, Funding acquisition. **Juan Andrés:** Conceptualization, Writing – review & editing, Supervision, Resources, Funding acquisition. **Elson Longo:** Conceptualization, Writing – review & editing, Supervision, Resources, Funding acquisition.

Declaration of competing interest

The authors declare that they have no known competing financial interests or personal relationships that could have appeared to influence the work reported in this paper.

Acknowledgments

The authors acknowledge the financial support of the Brazilian research financing institutions: Fundação de Amparo à Pesquisa do Estado de São Paulo (FAPESP; Grant Nos. 2013/07296-2, 19/23488-5, 2019/03722-3, 2019/25944-8, and 2019/23488-5), Coordenação de Aperfeiçoamento de Pessoal de Nível Superior - Brasil (CAPES) - Finance Code 001 and Conselho Nacional de Desenvolvimento Científico e Tecnológico (CNPq, 142035/2017-3). J.A. acknowledges Universitat Jaume I (project UJI-B2019-30), and the Ministerio de Ciencia, Innovación y Universidades (Spain) (project PGC2018094417-B-I00) for financially supporting this research.

Appendix A. Supplementary data

Supplementary data to this article can be found online at https://doi.org/10.1016/j.matchemphys.2022.125710.

References

[1] J. Low, J. Yu, M. Jaroniec, S. Wageh, A.A. Al-Ghamdi, Heterojunction photocatalysts, Adv. Mater. 29 (2017) 1–20.
[2] C. Byrne, G. Subramanian, S.C. Pillai, Recent advances in photocatalysis for environmental applications, J. Environ. Chem. Eng. 6 (2018) 3531–3555.
[3] X. Li, J. Li, J. Bai, Y. Dong, L. Li, B. Zhou, The inhibition effect of tert-butyl alcohol on the TiO_2 nano assays photoelectrocatalytic degradation of different organics and its mechanism, Nano-Micro Lett. 8 (2016) 221–231.
[4] Q.Z. Bocheng Qiu, Mengmeng Du, Linggang Fan, Mingyang Xing, Jinlong Zhang, Efficient solar light harvesting CdS/Co_9S_8 hollow cubes for Z-scheme photocatalytic water splitting, Angew. Chem. Int. Ed. 56 (2017) 2684–2688.
[5] Y. Bai, Y. Zhou, J. Zhang, X. Chen, Y. Zhang, J. Liu, J. Wang, F. Wang, C. Chen, C. Li, R. Li, C. Li, Homophase junction for promoting spatial charge separation in photocatalytic water splitting, ACS Catal. 9 (2019) 3242–3252.
[6] Q. Wang, M. Nakabayashi, T. Hisatomi, S. Sun, S. Akiyama, Z. Wang, Z. Pan, X. Xiao, T. Watanabe, T. Yamada, N. Shibata, T. Takata, K. Domen, Oxysulfide photocatalyst for visible-light-driven overall water splitting, Nat. Mater. 18 (2019) 827–832.
[7] Y. Wang, H. Suzuki, J. Xie, O. Tomita, D.J. Martin, M. Higashi, D. Kong, R. Abe, J. Tang, Mimicking natural photosynthesis: solar to renewable H_2 fuel synthesis by Z-scheme water splitting systems, Chem. Rev. 118 (2018) 5201–5241.
[8] M.N. Mario Bartsch, The role of interfaces in heterostructures, ChemPlusChem 82 (2017) 42–59, 2017.
[9] X. Lin, J. Hou, X. Guo, Y. Wang, J. Zheng, C. Liu, Y. Yang, G. Che, Heterostructured Ag_3PO_4/Ag/Bi $_{3.64}Mo_{0.36}O_{6.55}$ nanospheres with enhanced photocatalytic activity under visible light irradiation, Separ. Purif. Technol. 156 (2015) 875–880.
[10] F. Chen, Q. Yang, X. Li, G. Zeng, D. Wang, C. Niu, J. Zhao, H. An, T. Xie, Y. Deng, Hierarchical assembly of graphene-bridged Ag_3PO_4/Ag/$BiVO_4$ (040) Z-scheme photocatalyst: an efficient, sustainable and heterogeneous catalyst with enhanced visible-light photoactivity towards tetracycline degradation under visible light irradiation, Appl. Catal. B Environ. 200 (2017) 330–342.
[11] Z. Wang, T. Hu, K. Dai, J. Zhang, C. Liang, Construction of Z-scheme Ag_3PO_4/Bi_2WO_6 composite with excellent visible-light photodegradation activity for removal of organic contaminants, Chin. J. Catal. 38 (2017) 2021–2029.
[12] J. Lu, Y. Wang, F. Liu, L. Zhang, S. Chai, Fabrication of a direct Z-scheme type WO_3/Ag_3PO_4 composite photocatalyst with enhanced visible-light photocatalytic performances, Appl. Surf. Sci. 393 (2017) 180–190.
[13] C. Ayappan, V. Jayaraman, B. Palanivel, A. Pandikumar, A. Mani, Facile preparation of novel Sb_2S_3 nanoparticles/rod-like α-Ag_2WO_4 heterojunction photocatalysts: continuous modulation of band structure towards the efficient removal of organic contaminants, Separ. Purif. Technol. 236 (2020) 116302.
[14] J.S. da Silva, T.R. Machado, A.B. Trench, A.D. Silva, V. Teodoro, P.C. Vieira, T. A. Martins, E. Longo, Enhanced photocatalytic and antifungal activity of hydroxyapatite/α-$AgVO_3$ composites, Mater. Chem. Phys. 252 (2020) 123294.
[15] S. Rajamohan, V. Kumaravel, R. Muthuramalingam, S. Ayyadurai, A. Abdel-Wahab, B. Sub Kwak, M. Kang, S. Sreekantan, Fe_3O_4–Ag_2WO_4: facile synthesis, characterization and visible light assisted photocatalytic activity, New J. Chem. 41 (2017) 11722–11730.
[16] A. Hezam, J. Wang, Q.A. Drmosh, P. Karthik, M. Abdullah Bajiri, K. Namratha, M. Zare, T.R. Lakshmeesha, S. Shivanna, C. Cheng, B. Neppolian, K. Byrappa, Rational construction of plasmonic Z-scheme Ag-ZnO-CeO_2 heterostructures for highly enhanced solar photocatalytic H2 evolution, Appl. Surf. Sci. 541 (2021) 148457.
[17] C. Ayappan, B. Palanivel, V. Jayaraman, T. Maiyalagan, A. Mani, One-step hydrothermal synthesis of $CaWO_4$/α-Ag_2WO_4 heterojunction: an efficient photocatalyst for removal of organic contaminants, Mater. Sci. Semicond. Process. 104 (2019) 104693.
[18] D. Sudha, P. Sivakumar, Review on the photocatalytic activity of various composite catalysts, Chem. Eng. Process: Process Intensification 97 (2015) 112–133.
[19] E.K.K. Kar, Composite Materials Processing, Applications, Characterizations, Springer-Verlag Berlin, 2017.

[20] J. Ge, Y. Zhang, Y.-J. Heo, S.-J. Park, Advanced design and synthesis of composite photocatalysts for the remediation of wastewater: a review, Catalysts 9 (2019) 122.

[21] S. Bera, D.-I. Won, S.B. Rawal, H.J. Kang, W.I. Lee, Design of visible-light photocatalysts by coupling of inorganic semiconductors, Catal. Today 335 (2019) 3–19.

[22] B. Shao, X. Liu, Z. Liu, G. Zeng, Q. Liang, C. Liang, Y. Cheng, W. Zhang, Y. Liu, S. Gong, A novel double Z-scheme photocatalyst $Ag_3PO_4/Bi_2S_3/Bi_2O_3$ with enhanced visible-light photocatalytic performance for antibiotic degradation, Chem. Eng. J. 368 (2019) 730–745.

[23] Z. Liu, Y. Jiang, X. Liu, G. Zeng, B. Shao, Y. Liu, Y. Liu, W. Zhang, W. Zhang, M. Yan, X. He, Silver chromate modified sulfur doped graphitic carbon nitride microrod composites with enhanced visible-light photoactivity towards organic pollutants degradation, Compos. B Eng. 173 (2019) 106918.

[24] T. Wu, X. Liu, Y. Liu, M. Cheng, Z. Liu, G. Zeng, B. Shao, Q. Liang, W. Zhang, Q. He, W. Zhang, Application of QD-MOF composites for photocatalysis: energy production and environmental remediation, Coord. Chem. Rev. 403 (2020) 213097.

[25] S. Kumar, K. Ojha, A.K. Ganguli, Interfacial charge transfer in photoelectrochemical processes, Adv. Mater. Interfac. 4 (2017) 1600981.

[26] W. Hou, S.B. Cronin, A review of surface plasmon resonance-enhanced photocatalysis, Adv. Funct. Mater. 23 (2013) 1612–1619.

[27] K. Ueno, H. Misawa, Surface plasmon-enhanced photochemical reactions, J. Photochem. Photobiol. C Photochem. Rev. 15 (2013) 31–52.

[28] X. Bai, R. Zong, C. Li, D. Liu, Y. Liu, Y. Zhu, Enhancement of visible photocatalytic activity via Ag@C_3N_4 core–shell plasmonic composite, Appl. Catal. B Environ. 147 (2014) 82–91.

[29] F.A. Sofi, K. Majid, O. Mehraj, The visible light driven copper based metal-organic-framework heterojunction:HKUST-1@Ag-Ag_3PO_4 for plasmon enhanced visible light photocatalysis, J. Alloys Compd. 737 (2018) 798–808.

[30] F.A. Sofi, K. Majid, Plasmon induced interfacial charge transfer across Zr-based metal-organic framework coupled Ag_2WO_4 heterojunction functionalized by Ag NPs: efficient visible light photocatalyst, Chem. Phys. Lett. 720 (2019) 7–14.

[31] J. Li, F. Liu, Y. Li, Fabrication of an Ag/Ag_2MoO_4 plasmonic photocatalyst with enhanced photocatalytic performance for the degradation of ciprofloxacin, New J. Chem. 42 (2018) 12054–12061.

[32] Y. Song, W. Xie, C. Yang, D. Wei, X. Su, L. Li, L. Wang, J. Wang, Humic acid-assisted synthesis of Ag/Ag_2MoO_4 and Ag/Ag_2WO_4 and their highly catalytic reduction of nitro- and azo-aromatics, J. Mater. Res. Technol. 9 (2020) 5774–5783.

[33] Z. Xia, J. Min, S. Zhou, H. Ma, B. Zhang, X. Tang, Photocatalytic performance and antibacterial mechanism of Cu/Ag-molybdate powder material, Ceram. Int. 47 (2021) 12667–12679.

[34] X. Zhou, G. Liu, J. Yu, W. Fan, Surface plasmon resonance-mediated photocatalysis by noble metal-based composites under visible light, J. Mater. Chem. 22 (2012) 21337.

[35] G.M. Faccin, M.A. San-Miguel, J. Andres, E. Longo, E.Z. da Silva, Computational modeling for the Ag nanoparticle coalescence process: a case of surface plasmon resonance, J. Phys. Chem. C 121 (2017) 7030–7036.

[36] E.Z. da Silva, G.M. Faccin, T.R. Machado, N.G. Macedo, M. de Assis, S. Maya-Johnson, J.C. Sczancoski, J. Andrés, E. Longo, M.A. San-Miguel, Connecting theory with experiment to understand the sintering processes of Ag nanoparticles, J. Phys. Chem. C 123 (2019) 11310–11318.

[37] J. Andrés, A.F. Gouveia, L. Gracia, E. Longo, G. Manzeppi Faccin, E.Z. da Silva, D. H. Pereira, M.A. San-Miguel, Formation of Ag nanoparticles under electron beam irradiation: atomistic origins from first-principles calculations, Int. J. Quant. Chem. 118 (2018), e25551.

[38] K. Nubla, N. Sandhyarani, Ag nanoparticles anchored Ag_2WO_4 nanorods: an efficient methanol tolerant and durable Pt free electro-catalyst toward oxygen reduction reaction, Electrochim. Acta 340 (2020) 135942.

[39] A. Koyappayil, S. Berchmans, M.H. Lee, Dual enzyme-like properties of silver nanoparticles decorated Ag_2WO_4 nanorods and its application for H_2O_2 and glucose sensing, Colloids Surf. B Biointerfaces 189 (2020) 110840.

[40] M. Assis, E. Cordoncillo, R. Torres-Mendieta, H. Beltran-Mir, G. Minguez-Vega, R. Oliveira, E.R. Leite, C.C. Foggi, C.E. Vergani, E. Longo, J. Andres, Towards the scale-up of the formation of nanoparticles on alpha-Ag_2WO_4 with bactericidal properties by femtosecond laser irradiation, Sci. Rep. 8 (2018) 1884.

[41] N.G. Macedo, T.R. Machado, R.A. Roca, M. Assis, C.C. Foggi, V. Puerto-Belda, G. Mínguez-Vega, A. Rodrigues, M.A. San-Miguel, E. Cordoncillo, H. Beltrán-Mir, J. Andrés, E. Longo, Tailoring the bactericidal activity of Ag nanoparticles/α-Ag_2WO_4 composite induced by electron beam and femtosecond laser irradiation: integration of experiment and computational modeling, ACS Applied Bio Materials 2 (2019) 824–837.

[42] P.S.S. Lemos, G. S, R.A. Roca, M. Assis, R. Torres-Mendieta, H. Beltrán-Mir, G. C. Mínguez, E. Vega, J. Andrés, E. Longo, Laser and electron beam-induced formation of Ag/Cr structures on Ag_2CrO_4, Phys. Chem. Chem. Phys. 21 (2019) 6101–6111.

[43] C.-G.N. Hai Guo, Lei Zhang, Xiao-Ju Wen, Chao Liang, Xue-Gang Zhang, Dan-Lin Guan, Ning Tang, Guangming Zeng, Construction of direct Z-scheme AgI/$Bi_2Sn_2O_7$ nanojunction system with enhanced photocatalytic activity: accelerated interfacial charge transfer induced efficient Cr(VI) reduction, tetracycline degradation and Escherichia coli inactivation, ACS Sustain. Chem. Eng. 6 (2018) 8003–8018.

[44] D. Liu, W. Huang, L. Li, L. Liu, X. Sun, B. Liu, B. Yang, C. Guo, Experimental and theoretical investigation on photocatalytic activities of 1D Ag/Ag_2WO_4 nanostructures, Nanotechnology 28 (2017) 385702.

[45] J. Paulo de Campos da Costa, M. Assis, V. Teodoro, A. Rodrigues, C. Cristina de Foggi, M.A. San-Miguel, J.P. Pereira do Carmo, J. Andrés, E. Longo, Electron beam irradiation for the formation of thick Ag film on Ag_3PO_4, RSC Adv. 10 (2020) 21745–21753.

[46] G. Botelho, J.C. Sczancoski, J. Andres, L. Gracia, E. Longo, Experimental and theoretical study on the structure, optical properties, and growth of metallic silver nanostructures in Ag_3PO_4, J. Phys. Chem. C 119 (2015) 6293–6306.

[47] T. Yan, W. Guan, Y. Xiao, J. Tian, Z. Qiao, H. Zhai, W. Li, J. You, Effect of thermal annealing on the microstructures and photocatalytic performance of silver orthophosphate: the synergistic mechanism of Ag vacancies and metallic Ag, Appl. Surf. Sci. 391 (2017) 592–600.

[48] Z. Liu, Y. Liu, P. Xu, Z. Ma, J. Wang, H. Yuan, Rational design of wide spectral-responsive heterostructures of Au nanorod coupled Ag_3PO_4 with enhanced photocatalytic performance, ACS Appl. Mater. Interfaces 9 (2017) 20620–20629.

[49] S. Linic, P. Christopher, D.B. Ingram, Plasmonic-metal nanostructures for efficient conversion of solar to chemical energy, Nat. Mater. 10 (2011) 911–921.

[50] A.B. Trench, T.R. Machado, A.F. Gouveia, M. Assis, L.G. da Trindade, C. Santos, A. Perrin, C. Perrin, M. Oliva, J. Andrés, E. Longo, Connecting structural, optical, and electronic properties and photocatalytic activity of Ag_3PO_4:Mo complemented by DFT calculations, Appl. Catal. B Environ. 238 (2018) 198–211.

[51] A.F.G. Roman Alvarez-Roca, Camila Cristina de Foggi, Pablo Santana Lemos, Lourdes Gracia, Luís Fernando da Silva, Carlos Eduardo Vergani, Miguel San-Miguel, Elson Longo, and Juan Andrés, Selective Synthesis of α-, β-, and γ-Ag_2WO_4 Polymorphs: promising Platforms for Photocatalytic and Antibacterial Materials, Inorg. Chem. 60 (2021) 1062–1079.

[52] R. Masse, I. Tordjman, A. Durif, Refinement of crystal-structure of silver monophosphate, Ag_3PO_4-existence of high-temperature form, Zeitschrift Fur Kristallographie 144 (1976) 76–81.

[53] S.G.P.M. Skarstad, $(W_4O_{16})^{8-}$ polyion IN the high temperature modification OF silver tungstate, Mater. Res. Bull. 10 (1975) 791–800.

[54] T. Cai, W. Zeng, Y. Liu, L. Wang, W. Dong, H. Chen, X. Xia, A promising inorganic-organic Z-scheme photocatalyst Ag_3PO_4/PDI supermolecule with enhanced photoactivity and photostability for environmental remediation, Appl. Catal. B Environ. 263 (2020) 118327.

[55] J. Huang, D. Li, Y. Liu, R. Li, P. Chen, H. Liu, W. Lv, G. Liu, Y. Feng, Ultrathin Ag_2WO_4-coated P-doped g-C_3N_4 nanosheets with remarkable photocatalytic performance for indomethacin degradation, J. Hazard Mater. 392 (2020) 122355.

[56] G.W. Hao Zhang, Da Chen, Xiaojun Lv, Jinghong Li, Tuning photoelectrochemical performances of Ag-TiO_2 nanocomposites via reduction/oxidation of Ag, Chem. Mater. 20 (2008) 6543–6549.

[57] Y. Liu, L. Fang, H. Lu, Y. Li, C. Hu, H. Yu, One-pot pyridine-assisted synthesis of visible-light-driven photocatalyst Ag/Ag_3PO_4, Appl. Catal. B Environ. 115–116 (2012) 245–252.

[58] C. Zhang, K. Yu, Y. Feng, Y. Chang, T. Yang, Y. Xuan, D. Lei, L.-L. Lou, S. Liu, Novel 3DOM-$SrTiO_3$/Ag/Ag_3PO_4 ternary Z-scheme photocatalysts with remarkably improved activity and durability for contaminant degradation, Appl. Catal. B Environ. 210 (2017) 77–87.

[59] D.H. Yoon, Y.J. Tak, S.P. Park, J. Jung, H. Lee, H.J. Kim, Simultaneous engineering of the interface and bulk layer of Al/sol-NiOx/Si structured resistive random access memory devices, J. Mater. Chem. C 2 (2014) 6148–6154.

[60] B. Sasi, K.G. Gopchandran, Nanostructured mesoporous nickel oxide thin films, Nanotechnology 18 (2007) 115613.

[61] P. Castillero, V. Rico-Gavira, C. López-Santos, A. Barranco, V. Pérez-Dieste, C. Escudero, J.P. Espinós, A.R. González-Elipe, formation of subsurface W^{5+} species in gasochromic Pt/WO_3 thin films exposed to hydrogen, J. Phys. Chem. C 121 (2017) 15719–15727.

[62] S. Koohfar, A.B. Georgescu, I. Hallsteinsen, R. Sachan, M.A. Roldan, E. Arenholz, D. P. Kumah, Effect of strain on magnetic and orbital ordering of $LaSrCrO_3$/$LaSrMnO_3$ heterostructures, Phys. Rev. B (2020) 101.

[63] Z. Wu, X. Chen, E. Mu, Y. Liu, Z. Che, C. Dun, F. Sun, X. Wang, Y. Zhang, Z. Hu, Lattice strain enhances thermoelectric properties in Sb_2Te_3/Te heterostructure, Adv. Electron. Mater. 6 (2019) 1900735.

[64] Y. Tian, Q. Zheng, J. Zhao, Tensile strain-controlled photogenerated carrier dynamics at the van der Waals heterostructure interface, J. Phys. Chem. Lett. 11 (2020) 586–590.

[65] P. Jiang, M.-C. Record, P. Boulet, First-principles calculations on $CuInSe_2$/AlP heterostructures, J. Mater. Chem. C 8 (2020) 4732–4742.

[66] H.T. Kung, P. Li, J.J. Lee, Y. Zhao, A. Dumont, Z.H. Lu, Reaction and energy levels at oxide–oxide heterojunction interfaces, Adv. Mater. Interfac. 6 (2019) 1901456.

[67] D.L. Wood, J. Tauc, Weak absorption tails in amorphous semiconductors, Phys. Rev. B 5 (1972) 3144–3151.

[68] G. Botelho, J. Andres, L. Gracia, L.S. Matos, E. Longo, Photoluminescence and photocatalytic properties of Ag_3PO_4 microcrystals: an experimental and theoretical investigation, ChemPlusChem 81 (2016) 202–212.

[69] M. Ge, Z. Li, Recent progress in Ag_3PO_4 -based all-solid-state Z-scheme photocatalytic systems, Chin. J. Catal. 38 (2017) 1794–1803.

[70] F.X. Nobre, I.S. Bastos, R.O. Dos Santos Fontenelle, E.A.A. Junior, M.L. Takeno, L. Manzato, J.M.E. de Matos, P.P. Orlandi, J. de Fatima Souza Mendes, W.R. Brito, P.R. da Costa Couceiro, Antimicrobial properties of alpha-Ag_2WO_4 rod-like microcrystals synthesized by sonochemistry and sonochemistry followed by hydrothermal conventional method, Ultrason. Sonochem. 58 (2019) 104620.

[71] J. Lv, K. Dai, J. Zhang, L. Lu, C. Liang, L. Geng, Z. Wang, G. Yuan, G. Zhu, In situ controllable synthesis of novel surface plasmon resonance-enhanced Ag_2WO_4/Ag/Bi_2MoO_6 composite for enhanced and stable visible light photocatalyst, Appl. Surf. Sci. 391 (2017) 507–515.

[72] T. Simon, N. Bouchonville, M.J. Berr, A. Vaneski, A. Adrovic, D. Volbers, R. Wyrwich, M. Doblinger, A.S. Susha, A.L. Rogach, F. Jackel, J.K. Stolarczyk,

J. Feldmann, Redox shuttle mechanism enhances photocatalytic H_2 generation on Ni-decorated CdS nanorods, Nat. Mater. 13 (2014) 1013–1018.
[73] L. Wang, J. Ding, Y. Chai, Q. Liu, J. Ren, X. Liu, W.L. Dai, CeO_2 nanorod/g-C_3N_4/N-rGO composite: enhanced visible-light-driven photocatalytic performance and the role of N-rGO as electronic transfer media, Dalton Trans. 44 (2015) 11223–11234.
[74] C. Tang, E. Liu, J. Wan, X. Hu, J. Fan, Co_3O_4 nanoparticles decorated Ag_3PO_4 tetrapods as an efficient visible-light-driven heterojunction photocatalyst, Appl. Catal. B Environ. 181 (2016) 707–715.
[75] A. Phuruangrat, N. Ekthammathat, S. Thongtem, T. Thongtem, Preparation of $LaPO_4$ nanowires with high aspect ratio by a facile hydrothermal method and their photoluminescence, Res. Chem. Intermed. 39 (2012) 1363–1371.
[76] P.F.S. Pereira, C.C. Santos, A.F. Gouveia, M.M. Ferrer, I.M. Pinatti, G. Botelho, J. R. Sambrano, I.L.V. Rosa, J. Andrés, E. Longo, α-Ag_2–2xZnxWO_4 ($0 \leq x \leq 0.25$) solid solutions: structure, morphology, and optical properties, Inorg. Chem. 56 (2017) 7360–7372.
[77] E. Longo, D.P. Volanti, V.M. Longo, L. Gracia, I.C. Nogueira, M.A.P. Almeida, A. N. Pinheiro, M.M. Ferrer, L.S. Cavalcante, J. Andrés, Toward an understanding of the growth of Ag filaments on α-Ag_2WO_4 and their photoluminescent properties: a combined experimental and theoretical study, J. Phys. Chem. C 118 (2014) 1229–1239.
[78] R.A. Roca, J.C. Sczancoski, I.C. Nogueira, M.T. Fabbro, H.C. Alves, L. Gracia, L.P. S. Santos, C.P. de Sousa, J. Andrés, G.E. Luz, E. Longo, L.S. Cavalcante, Facet-dependent photocatalytic and antibacterial properties of α-Ag_2WO_4 crystals: combining experimental data and theoretical insights, Catal. Sci. Technol. 5 (2015) 4091–4107.
[79] T. Li, H. Wei, H. Jia, T. Xia, X. Guo, T. Wang, L. Zhu, Mechanisms for highly efficient mineralization of bisphenol A by heterostructured Ag_2WO_4/Ag_3PO_4 under simulated solar light, ACS Sustain. Chem. Eng. 7 (2019) 4177–4185.
[80] N.R. Khalid, U. Mazia, M.B. Tahir, N.A. Niaz, M.A. Javid, Photocatalytic degradation of RhB from an aqueous solution using Ag_3PO_4/N-TiO_2 heterostructure, J. Mol. Liq. 313 (2020) 113522.
[81] X. Li, T. Wan, J. Qiu, H. Wei, F. Qin, Y. Wang, Y. Liao, Z. Huang, X. Tan, In-situ photocalorimetry-fluorescence spectroscopy studies of RhB photocatalysis over Z-scheme g-C_3N_4@Ag@Ag_3PO_4 nanocomposites: a pseudo-zero-order rather than a first-order process, Appl. Catal. B Environ. 217 (2017) 591–602.
[82] W. Cao, Y. An, L. Chen, Z. Qi, Visible-light-driven Ag_2MoO_4/Ag_3PO_4 composites with enhanced photocatalytic activity, J. Alloys Compd. 701 (2017) 350–357.
[83] R.K. Santos, T.A. Martins, G.N. Silva, M.V.S. Conceicao, I.C. Nogueira, E. Longo, G. Botelho, Ag_3PO_4/NiO composites with enhanced photocatalytic activity under visible light, ACS Omega 5 (2020) 21651–21661.
[84] N. Li, S. Miao, X. Zheng, J. Lai, S. Lv, X. Gu, M. Zhang, J. Yang, S. Cui, Construction of Ag_3PO_4/$BiNbO_4$ heterojunction photocatalysts with high activity for Rhodamine B removal under simulated sunlight irradiation, Ceram. Int. 45 (2019) 24260–24268.
[85] T. Zhou, G. Zhang, P. Ma, X. Qiu, H. Zhang, H. Yang, G. Liu, Efficient degradation of rhodamine B with magnetically separable Ag_3PO_4@$MgFe_2O_4$ composites under visible irradiation, J. Alloys Compd. 735 (2018) 1277–1290.
[86] A.B. Trench, T.R. Machado, A.F. Gouveia, C.C. Foggi, V. Teodoro, I. Sánchez-Montes, M.M. Teixeira, L.G. da Trindade, N. Jacomaci, A. Perrin, C. Perrin, J. M. Aquino, J. Andrés, E. Longo, Rational design of W-doped Ag_3PO_4 as an efficient antibacterial agent and photocatalyst for organic pollutant degradation, ACS Omega 5 (2020) 23808–23821.
[87] S. Li, S. Hu, W. Jiang, Y. Liu, J. Liu, Z. Wang, Facile synthesis of flower-like Ag_3VO_4/Bi_2WO_6 heterojunction with enhanced visible-light photocatalytic activity, J. Colloid Interface Sci. 501 (2017) 156–163.
[88] M. Sun, R. Senthil, J. Pan, S. Osman, A. Khan, A facile synthesis of visible-light driven rod-on-rod like α-FeOOH/α-$AgVO_3$ nanocomposite as greatly enhanced photocatalyst for degradation of rhodamine B, Catalysts 8 (2018) 392.
[89] S.K. Ray, D. Dhakal, S.W. Lee, Rapid degradation of naproxen by AgBr-α-$NiMoO_4$ composite photocatalyst in visible light: mechanism and pathways, Chem. Eng. J. 347 (2018) 836–848.
[90] H. Xu, Y. Cao, J. Xie, J. Hu, Y. Li, D. Jia, A construction of Ag-modified raspberry-like AgCl/Ag_2WO_4 with excellent visible-light photocatalytic property and stability, Mater. Res. Bull. 102 (2018) 342–352.
[91] H. Li, Y. Zhang, Q. Zhang, Y. Wang, Y. Fan, X. Gao, J. Niu, Boosting visible-light photocatalytic degradation of indomethacin by an efficient and photostable Ag_3PO_4/NG/WO_3 composites, Appl. Surf. Sci. 490 (2019) 481–491.
[92] U. Rafiq, O. Mehraj, S. Lone, M. Wahid, K. Majid, Solvothermal synthesis of Ag_2WO_4/Sb_2WO_6 heterostructures for enhanced charge transfer properties and efficient visible-light-driven photocatalytic activity and stability, J. Environ. Chem. Eng. 8 (2020) 104301.
[93] Y. Sang, X. Cao, G. Dai, L. Wang, Y. Peng, B. Geng, Facile one-pot synthesis of novel hierarchical Bi_2O_3/Bi_2S_3 nanoflower photocatalyst with intrinsic p-n junction for efficient photocatalytic removals of RhB and Cr(VI), J. Hazard Mater. 381 (2020) 120942.
[94] W. Shi, F. Guo, S. Yuan, In situ synthesis of Z-scheme Ag_3PO_4/$CuBi_2O_4$ photocatalysts and enhanced photocatalytic performance for the degradation of tetracycline under visible light irradiation, Appl. Catal. B Environ. 209 (2017) 720–728.
[95] X. Yang, H. Tang, J. Xu, M. Antonietti, M. Shalom, Silver phosphate/graphitic carbon nitride as an efficient photocatalytic tandem system for oxygen evolution, ChemSusChem 8 (2015) 1350–1358.
[96] E. Abroshan, S. Farhadi, A. Zabardasti, Novel magnetically separable Ag_3PO_4/$MnFe_2O_4$ nanocomposite and its high photocatalytic degradation performance for organic dyes under solar-light irradiation, Sol. Energy Mater. Sol. Cell. 178 (2018) 154–163.